

Georeferencing with Self-Calibration for Airborne Full-Waveform Lidar Data Using Digital Elevation Model

Qinghua Li and Jie Shan

Abstract

Precise georeferencing of airborne full-waveform lidar is a complex process. On one hand, no ground control points are visible due to heavy canopy. While on the other hand, precise georeferencing relies on ground control. As an alternative, we propose to use an available digital elevation model (DEM) as control. The mathematical framework minimizes the difference between the lidar DEM and the reference DEM. Our solution consists of two steps: initial optimization to find reliable ground points through iterative filtering and georeferencing, and fine optimization to achieve precise georeferencing and lidar system calibration. Through this approach, the waveform-derived DEM can best fit the reference DEM, with a mean of 0.937 m and standard deviation of 0.792 m, while the time-synchronization offset and boresight angles are simultaneously determined, i.e., self-calibrated. This development provides a novel georeferencing approach with self-calibration for lidar data without using conventional ground control points.

Introduction

In lidar data processing, georeferencing is the process by which the 3D points in the laser-scanner coordinate system are transformed into the 3D points in a mapping coordinate system. During this transform, the measurements from positioning and orientation systems (POS) as well as the relative position and orientation between the onboard components of the laser scanner and POS are used.

In most cases, the lidar and POS are independent units from different manufacturers. The accuracy of the georeferenced data depends on synchronization and calibration of the lidar and POS. During the process of georeferencing, calibration means the determination of the exterior orientation described by boresight misalignment angles (Shan and Toth 2018). For this purpose, ground control points (Pothou *et al.* 2008), boresight flight plan (Skaloud and Schaer 2007), and multiple overlapping flight stripes (Zhang *et al.* 2015) are commonly required in conventional calibration methods.

The lidar system can be calibrated before or after the data are collected. Conventionally, the manufacturer or data provider will precalibrate the system parameters prior to data collection. Such preflight calibration is often conducted in a lab and needs hardware, on-site measurement, and ground truth. For example, Jung *et al.* (2015) used a specifically designed double-deck calibration facility to calibrate a kinematic 3D laser scanning system. Morales *et al.* (2014) calibrated the boresight parameters by iteratively maximizing both the flatness and the area of

visible planes such as room corners. Sun and Neumann (2015) described calibration on the basis of both ground testing and a few in-flight measurements. Nagarajan and Moafipoor (2018) performed feature-based registration in a lab facility utilizing static data to determine the boresight misalignment by minimizing the volume formed between low-point-density lidar and control planes. Cortes, Shahbazi, and Ménard (2018) formed a calibration test field with different planes and cylindrical concrete pillars, and used unscented particle filtering to integrate the inertial measurement unit (IMU) measurements with lidar observations. Since the cost of such lab-based calibration is usually very high, it is often not practical. Furthermore, and more critical, results from lab calibration may considerably vary during flight, necessitating in-flight or postflight calibration.

Researchers have developed algorithms to calibrate systems after the data are delivered. Toth, Csanyi, and Grejner-Brzezinska (2002) used two/three or more overlapping lidar stripes flown in a certain pattern and made use of observable horizontal and vertical discrepancies between the different lidar data sets to determine the unknown misalignment angles. Skaloud and Lichti (2006) developed an automated lidar boresight self-calibration for urban areas where buildings are separated and have a relatively simple roof structure. Chen *et al.* (2012) calibrated the boresight misalignment by combining adjustment between lidar point clouds and aerial images. The tie points in overlapping areas are selected, and the boresight misalignment is removed by minimizing the distances between the image points selected manually and those projected from ground points. Hebel and Stilla (2012) extracted planar shapes with a region-growing approach and a random-sample consensus segmentation method and transferred the planarity constraints into systems of linear equations to determine both the boresight parameters and the data alignment. Zhang *et al.* (2015) aerotriangulated aerial images covering the same area as lidar stripes and used them as the reference data for lidar stripe adjustment. Le Gentil, Vidal-Calleja, and Huang (2018) used a set of planes as a calibration target and minimized the lidar point-to-plane distances to jointly calibrate and localize the system. Zhu *et al.* (2018) extracted key points and built feature descriptors based on the neighborhood normal vector, point-cloud density, and curvature for lidar point-cloud registration. Liu and Li (2019) proposed incorporating cone and cylinder features instead of planar features for lidar-IMU system calibration. For a single-photon lidar system (Q. Li *et al.* 2016), Pan, Hartzell, and Glennie (2017) adapted a rigorous plane-based calibration algorithm to incorporate a circular scan pattern and augmented a prism-wedge-angle parameter

Qinghua Li and Jie Shan are with the Lyles School of Civil Engineering, Purdue University, West Lafayette, IN 47907 (qinghua.li.1@purdue.edu; Jie Shan, jshan@purdue.edu).

Qinghua Li is with the Northwestern Institute on Complex Systems (NICO), Northwestern University, Evanston, IL, 60208 (qinghua.li@kellogg.northwestern.edu)

Photogrammetric Engineering & Remote Sensing
Vol. 87, No. 1, January 2021, pp. 43–52.
0099-1112/20/43–52

© 2021 American Society for Photogrammetry
and Remote Sensing
doi: 10.14358/PERS.87.1.43

to model wedge wobble and other correlated errors. In lunar topographic mapping (Wu and Liu 2017), the boresight offsets were improved based on a geometric model through a least-squares adjustment by triple-matching tie points between the narrow-angle camera images.

Postflight calibration is desired because the quality of the data may be significantly improved. However, the conventional calibration methods have a few limitations. For example, multiple stripes (Toth *et al.* 2002; Chen *et al.* 2012; Zhang *et al.* 2015; Zhu *et al.* 2018) or circular scans (Pan *et al.* 2017) of lidar points acquired from the same platform are necessary to conduct the calibration. Also, a significant number of planar or regular-shaped objects are usually required (Skaloud and Lichti 2006; Hebel and Stilla 2012; Le Gentil *et al.* 2018; Liu and Li 2019). It becomes fairly challenging when no exact correspondence of ground control points exists in the lidar point cloud. For example, full-waveform lidar data (Q. Li *et al.* 2016; Li *et al.* 2018) are widely applied in forest studies (Pirotti 2011; Hancock *et al.* 2015; White *et al.* 2016; Guo *et al.* 2017), where it is difficult to find regular-shaped objects to meet the requirement of postflight calibration. One of the solutions to the problem of insufficient or no corresponding ground controls is to manually deploy lidar-specific ground targets (Csanyi and Toth 2007). The other approach is to estimate the parameters through Bayesian estimation (Luo, Liu, and Liu 2010). However, they require additional fieldwork or good prior knowledge about the sensor orientation and position.

This article presents a new approach to calibrating system parameters of a lidar system with full-waveform lidar data. In this new development, only a publicly accessible (bare-ground) digital elevation model (DEM) is utilized as the control over a study area without point-to-point correspondence (Shan, 2001; Cao *et al.* 2019). There is no need for conventional ground control points, reflective targets, or planar ground or objects. We model the calibration task as an optimization problem that minimizes the difference between the lidar-generated DEM and the reference DEM. Working with a DEM relieves the need for conventional ground control points or specifically designed multiple flight stripes. As a result of this development, the coupled task of lidar data georeferencing and lidar system calibration can be carried out under one unified self-calibration mathematical model. The new calibration approach can be implemented and routinely conducted for full-waveform or discrete lidar systems.

Mathematical Models

In this section, we will introduce the mathematical model of georeferencing and its related parameters, which will be resolved through an optimization strategy in the next section. The flowchart of the proposed method is shown in Figure 1. It consists of two general steps: finding stable ground points and then using them to register the waveform lidar point cloud to the reference DEM.

It should be noted that the problem we are dealing with is not conventional. For full-waveform lidar data, a waveform record will be decomposed to one or multiple waveform components (Q. Li *et al.* 2016), each of which corresponds to a lidar point in the laser-scanner frame. A lidar system contains three coordinate systems: the mapping frame, the laser frame, and the IMU frame. Our georeferencing task is to transform the lidar point cloud from the scanner frame to the mapping frame using the POS measurements and the reference DEM. The model of such a transform must consider the boresight angles of the laser scanner and potential systematic errors in the POS measurements. The difficulty of the problem is that the waveform lidar point cloud is over canopy, and there are no visible ground control points in the data set. What we have as a control is only a reference DEM. Therefore, we need to find ground points from the waveform lidar point clouds, which

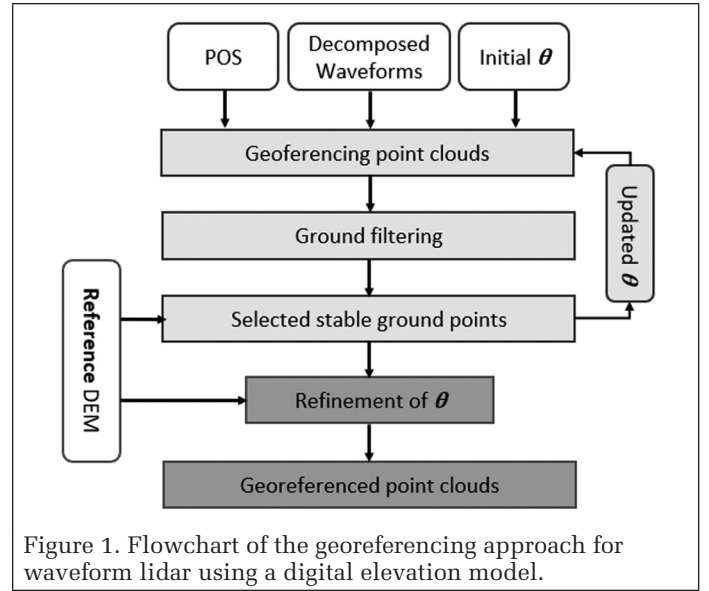


Figure 1. Flowchart of the georeferencing approach for waveform lidar using a digital elevation model.

in turn are dependent on the unknown boresight angles. This is a unique situation where ground filtering and georeferencing are coupled or interdependent. As shown in Figure 1, iteration must be involved.

Direct Georeferencing

We start from using lidar and POS measurements to directly georeference the lidar data, which is the first step toward final, precise georeferencing. Direct georeferencing transforms the target's coordinates from the laser scanner's coordinate system to the mapping coordinate system. The transformation involves the IMU coordinate system and the horizontal coordinate system, which is a celestial coordinate system that uses the observer's local horizon as the fundamental plane. The whole process (Shan and Toth 2018) can be described as

$$\mathbf{r}_{\text{target}}^m(t_s, t_{\text{IMU}}) = \mathbf{r}_{\text{platform}}^m(t_{\text{IMU}}) + \mathbf{R}_H^m(t_{\text{IMU}}) \cdot \mathbf{R}_{\text{IMU}}^H(t_{\text{IMU}}) \cdot \mathbf{R}_S^{\text{IMU}} \cdot \mathbf{r}_{\text{target}}^S(t_s) \quad (1)$$

where $\mathbf{r}_{\text{target}}^m(t_s, t_{\text{IMU}})$ and $\mathbf{r}_{\text{target}}^S(t_s)$ are the coordinates in the mapping frame and the laser scanner's frame, respectively; $\mathbf{r}_{\text{platform}}^m(t_{\text{IMU}})$ is the position of the lidar platform; and $\mathbf{R}_H^m(t_{\text{IMU}})$, $\mathbf{R}_{\text{IMU}}^H(t_{\text{IMU}})$, and $\mathbf{R}_S^{\text{IMU}}$ are, respectively, the rotation matrices between the mapping frame and the horizontal frame, the horizontal frame and the IMU frame, and the IMU frame and the laser scanner's frame.

In Equation 1, there are two sets of variables that will be resolved in the following process of calibration. The first is the time misalignment $\Delta t = t_s - t_{\text{IMU}}$, where t_s and t_{IMU} are the clock time of the laser scanner and the POS unit, respectively. A synchronized system assumes $\Delta t = 0$ s; otherwise, Δt should be determined during the calibration process (Liu 2017). The second set of parameters is the boresight angles ($\Delta\omega$, $\Delta\phi$, $\Delta\kappa$, for roll, pitch, and yaw) in the time-invariant matrix $\mathbf{R}_S^{\text{IMU}}$. In the initial stage of direct georeferencing, these angles are assumed to be known, often either 0° or 90° depending on the specific definition of the onboard coordinate frames.

Calibration

In practice, the axes of the scanner's coordinate system and the navigation coordinate system are not parallel. The mounting misalignment angles ($\Delta\omega$, $\Delta\phi$, $\Delta\kappa$), if available from lab calibration, are used to perform the rotation between these two frames.

We take the problems of both synchronization and boresight calibration into consideration and define $\theta = [\Delta t, \Delta\omega, \Delta\phi, \Delta\kappa]$. The coordinate of a lidar point p in the mapping frame can be expressed as

$$\mathbf{r}_{\text{target},p}^m(\text{POS}_p, \mathbf{r}_{\text{target},p}^S; \boldsymbol{\theta}) = G\left[\left(\mathbf{r}_{\text{platform}}^m, \mathbf{R}_H^m, \mathbf{R}_{\text{IMU}}^H\right)_p, \mathbf{r}_{\text{target},p}^S; (\Delta t, \Delta\omega, \Delta\phi, \Delta\kappa)\right] = \mathbf{r}_{\text{platform}}^m(t_{S,p} - \Delta t) + \mathbf{R}_H^m(t_{S,p} - \Delta t) \mathbf{R}_{\text{IMU}}^H(t_{S,p} - \Delta t) \mathbf{R}_S^{\text{IMU}}(\Delta\omega, \Delta\phi, \Delta\kappa) \cdot \mathbf{r}_{\text{target},p}^S(t_S) \quad (2)$$

For the purpose of georeferencing, we propose using a known DEM as a replacement ground control (RGC) under the assumption that no significant terrain change happened between the time the reference DEM was produced and the time the new lidar data were collected.

Let $\{\cdot\}_N$ denote a set of N lidar points, which include both ground (p_{grnd}) and nonground (p_{nongrnd}) points; the objective function is the mean of squared deviation (MSD) or error (MSE) between a set of $N_{\text{grnd}}(\boldsymbol{\theta}_g)$ ground points and the reference DEM:

$$f_N(\boldsymbol{\theta}_G; \boldsymbol{\theta}_g) = \text{MSD}\left(\left\{\mathbf{r}_{\text{target},p_{\text{grnd}}(\boldsymbol{\theta}_g)}^m(\boldsymbol{\theta}_G)\right\}_{N_{\text{grnd}}(\boldsymbol{\theta}_g)}, \text{DEM}_{\text{ref}}\right) \quad (3)$$

Two sets of parameters are used in the calculation of the cost function: $\boldsymbol{\theta}_G$ is used to georeference the selected ground points according to Equation 2, and $\boldsymbol{\theta}_g$ is used to select ground points. The selection of the ground points is mostly based on traditional ground filtering.

Ground-Point Selection

First, the entire N lidar points $\{\mathbf{r}_{\text{target},p}^m\}_N$ are generated with $\boldsymbol{\theta}_g$. We then classify the points as ground or nonground using a ground filter implemented in LASSO software (<http://rapid-lasso.com/>), which uses a variation of the Axelsson (2000) triangulated irregular network refinement algorithm that avoids some of the trigonometry overhead. Once the mapping-frame ground points are labeled, their corresponding sensor-frame lidar points, together with the POS data, will be labeled. Finally, the sensor-frame ground points and

ground POS data, $\left\{\left(\mathbf{r}_{\text{target}}^m, \text{POS}\right)_{p_{\text{grnd}}(\boldsymbol{\theta}_g)}\right\}_{N_{\text{grnd}}(\boldsymbol{\theta}_g)}$, will be extracted

to generate a set of new ground points under $\boldsymbol{\theta}_G$.

The coordinates and selection of these RGC points come from different parameters $\boldsymbol{\theta}_G$ and $\boldsymbol{\theta}_g$. When $\boldsymbol{\theta}_g \approx \boldsymbol{\theta}_G$, the filtering results are equivalent, so that

$$\{\cdot\}_{N_{\text{grnd}}(\boldsymbol{\theta}_g)} = \{\cdot\}_{N_{\text{grnd}}(\boldsymbol{\theta}_G)} \quad (4)$$

This assumption does not hold if $\boldsymbol{\theta}_g$ and $\boldsymbol{\theta}_G$ are far away from each other, because the geometry and relative position between the lidar points may change significantly and the filtering results vary. The classification error introduced by the ground filtering will inevitably affect the objective function. If the true ground points are $\left\{\mathbf{r}_{\text{target},p_{\text{grnd}}}^m\right\}_{N_{\text{grnd}}}$, the estimated RGC points can be expressed as

$$\left\{\mathbf{r}_{\text{target},p_{\text{grnd}}(\boldsymbol{\theta}_g)}^m(\boldsymbol{\theta}_G)\right\}_{N_{\text{grnd}}(\boldsymbol{\theta}_g)} = \left\{\mathbf{r}_{\text{target},p_{\text{grnd}}}^m(\boldsymbol{\theta}_G)\right\}_{N_{\text{grnd}}} - \epsilon^-(\boldsymbol{\theta}_g) + \epsilon^+(\boldsymbol{\theta}_g),$$

where

$$\epsilon^-(\boldsymbol{\theta}_g) = \left\{\mathbf{r}_{\text{target},p_{\text{nongrnd}}^{\epsilon 1}(\boldsymbol{\theta}_g)}^m(\boldsymbol{\theta}_G)\right\}_{N_{\epsilon 1}(\boldsymbol{\theta}_g)}; \epsilon^+(\boldsymbol{\theta}_g) = \left\{\mathbf{r}_{\text{target},p_{\text{grnd}}^{\epsilon 2}(\boldsymbol{\theta}_g)}^m(\boldsymbol{\theta}_G)\right\}_{N_{\epsilon 2}(\boldsymbol{\theta}_g)} \quad (5)$$

False negative $\epsilon^-(\boldsymbol{\theta}_g)$ is the set of ground points that are mistakenly classified as nonground points by the ground filter, and false positive $\epsilon^+(\boldsymbol{\theta}_g)$ is the set of nonground points that are mistakenly classified as ground points. Both $N_{\epsilon 1}(\boldsymbol{\theta}_g)$ and $N_{\epsilon 2}(\boldsymbol{\theta}_g)$ are variables of $\boldsymbol{\theta}_g$. An effective optimization strategy should consider the fact that not all points after ground filtering are actual ground points.

Solution Methods

This section will describe the solution method for Equation 3. It consists of two steps: initial optimization and fine optimization. With the objective function Equation 3, the process of self-calibration can be modeled as an optimization problem of minimizing $f_N(\boldsymbol{\theta}_G, \boldsymbol{\theta}_g)$:

$$\boldsymbol{\theta}_G^* = (\Delta t, \Delta\omega, \Delta\phi, \Delta\kappa)^* = \underset{\boldsymbol{\theta}_G}{\text{argmin}} f_N(\boldsymbol{\theta}_G; \boldsymbol{\theta}_g) = \underset{\boldsymbol{\theta}_G}{\text{argmin}} \text{MSD}\left(\left\{\mathbf{r}_{\text{target},p_{\text{grnd}}(\boldsymbol{\theta}_g)}^m(\boldsymbol{\theta}_G)\right\}_{N_{\text{grnd}}(\boldsymbol{\theta}_g)}, \text{DEM}_{\text{ref}}\right) \quad (6)$$

Solving the optimization problem of Equation 6 consists of three steps: initial optimization, synchronization, and bore-sight calibration. A heuristic optimization will be applied in the initial calibration. After a relatively small searching area around the optimal solution is located by the initial optimization, a fixed set of ground points is chosen in the objective function. A fine optimization can be then conducted in the subsequent step.

Initial Optimization

At the beginning of optimization, the initial value $\boldsymbol{\theta}_0$ may be far away from the optimum solution. The ground filtering should be conducted whenever $\boldsymbol{\theta}$ changes to avoid the classification errors introduced by the unsynchronized data and the misaligned boresight angles. In such a case, the filtering process is equivalent to a conventional ground filter that directly works on the lidar points. The objective function becomes

$$f_N(\boldsymbol{\theta}_G; \boldsymbol{\theta}_G) = \text{MSD}\left(\left\{\mathbf{r}_{\text{target},p_{\text{grnd}}(\boldsymbol{\theta}_G)}^m(\boldsymbol{\theta}_G)\right\}_{N_{\text{grnd}}(\boldsymbol{\theta}_G)}, \text{DEM}_{\text{ref}}\right) \quad (7)$$

A consideration of Equation 7 is that the set of the estimated RGC points $N_{\text{grnd}}(\boldsymbol{\theta}_G)$ will change as $\boldsymbol{\theta}_G$ changes. This will in turn affect the objective function. Therefore, the problem becomes nonconvex and cannot be solved by a gradient-based searching algorithm, so a global optimization method should be applied in this initial stage.

We use a heuristic optimization method of particle swarm optimization (PSO; Kenney 1995; Golbon-Haghighi *et al.* 2018; Li *et al.* 2018) to optimize the objective function $f_N(\boldsymbol{\theta}_G, \boldsymbol{\theta}_G)$. It makes few or no assumptions about the problem being optimized and can search very large spaces of candidate solutions. However, it does not guarantee an optimal solution (Poli 2008). The basic idea of particle swarm optimization can be expressed in the following. We randomly generate some initial solution candidates $\boldsymbol{\theta}_0 = \{\boldsymbol{\theta}_{0,1}, \boldsymbol{\theta}_{0,2}, \dots, \boldsymbol{\theta}_{0,M}\}$. We define these candidates as the population and an individual candidate as a particle. Next, each candidate evolves according to

$$\Delta\boldsymbol{\theta}_{i+1,d} = w\Delta\boldsymbol{\theta}_{i,d} + c_1r_1(\boldsymbol{\theta}_d^* - \boldsymbol{\theta}_{i,d}) + c_2r_2(\boldsymbol{\theta}_i^* - \boldsymbol{\theta}_{i,d}) \quad (8)$$

$$\boldsymbol{\theta}_{i+1,d} = \boldsymbol{\theta}_{i,d} + \Delta\boldsymbol{\theta}_{i+1,d} \quad (9)$$

where $\Delta\boldsymbol{\theta}_{i,d}$ is the particle velocity, $\boldsymbol{\theta}_d^*$ is the best value that candidate d has achieved so far, $\boldsymbol{\theta}_i^*$ is the best value obtained by any particle in the population, c_1 and c_2 are constant numbers of learning factors, and r_1 and r_2 are random numbers between 0 and 1.

The fitness of a particle is evaluated according to the objective function $f_N(\boldsymbol{\theta}_G, \boldsymbol{\theta}_G)$. The algorithm converges when the best candidate cannot be further improved within a given number of iterations.

One of the challenges of particle swarm optimization is that the cost of calculating $f_N(\boldsymbol{\theta}_G, \boldsymbol{\theta}_G)$ for each candidate $\boldsymbol{\theta}_G$ could be very high. As reported by Q. Li *et al.* (2016), it takes up to a few hours to obtain the DEM from the raw waveform

data. In particle swarm optimization, the number of candidate in each iteration could be as many as a few dozen, and it may need hundreds of iterations before the algorithm converges. From the aspect of time efficiency, a subset of the data will be selected to conduct the optimization.

Fine Optimization

Using the result of the initial optimization, we obtain the solution θ_{init} as a first approximation to the global optimal solution. The subsequent search process is expected to be conducted in a relatively small neighborhood on the objective function $f_N(\theta_G, \theta_{\text{init}})$. When the search range is narrowed down to a small region by particle swarm optimization, the output of ground filtering can be directly applied to select the RGC points so that the selection of the ground points is no longer a variable of θ_G . In this case, $\{p_{\text{grnd}}(\theta_{\text{init}})\} = \{p_{\text{grnd}}(\theta_G)\}$

or $\{r_{\text{target}, p_{\text{grnd}}(\theta_{\text{PSO}})}^m(\theta_G)\}_{N_{\text{grnd}}(\theta_{\text{PSO}})} = \{r_{\text{target}, p_{\text{grnd}}(\theta_G)}^m(\theta_G)\}_{N_{\text{grnd}}(\theta_G)}$, and the objective function becomes

$$f_N(\theta_G; \theta_{\text{init}}) = \text{MSD} \left(\{r_{\text{target}, p_{\text{grnd}}(\theta_{\text{PSO}})}^m(\theta_G)\}_{N_{\text{grnd}}(\theta_{\text{PSO}})}, \text{DEM} \right) \quad (10)$$

Comparing to Equation 7, the objective function in Equation 10 is evaluated on a fixed set of RGC points $\{p_{\text{grnd}}(\theta_{\text{init}})\}$. Since $\{N_{\text{grnd}}(\theta_{\text{init}})\}$ does not vary with reference to θ_G , and the selection of the RGC points will be stable, a convex optimization such as a quasi-Newton algorithm can be utilized to find out the local minima around the result of particle swarm optimization.

To further guarantee the correct convergence of the objective function, the problems of synchronization and boresight calibration are solved separately. The BFGS quasi-Newton algorithm (Broyden 1970; Fletcher 1970; Goldfarb 1970; Shanno 1970) is applied in each step. This process will be demonstrated through the following experiments.

Experimental Data

An airborne lidar system consisting of a Riegl Q680i waveform laser scanner, a GPS receiver, and an inertial navigation system (INS) was used to test the methodologies developed in this article. In the experiment, the x-axis of the lidar frame points to the nadir direction of the aircraft, the y-axis is the flight direction, and the z-axis is the wing-to-wing direction of the airplane. On the other hand, the x-axis of the IMU frame points to the flight direction, the y-axis is the wing-to-wing direction of the airplane, and the z-axis points to the nadir direction of the aircraft (see Figure 2 for an illustration).

The full-waveform lidar data collected by the laser scanner are decomposed with a fuzzy mean-shift approach (Q. Li *et al.* 2016) to generate the discrete sensor-frame lidar points $\{r_{\text{target}, p}^s\}$. The GPS and

the INS are measured at different sampling rates and will be integrated and interpolated. At the same time, the integrated results are converted to the laser frame, i.e., the body frame. The conversion requires knowledge of the two distances between the origin of the body frame and the IMU frame. Specifically, the distance between the GPS antenna and the laser scanner is defined as the GPS lever arm and the distance between the IMU instrument and the laser scanner is the IMU

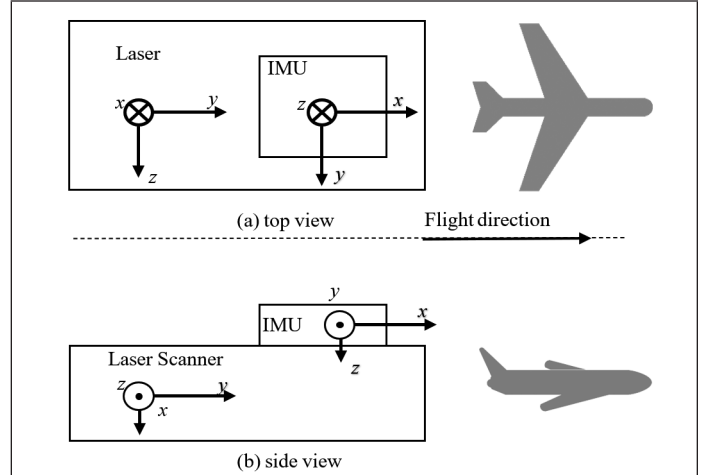


Figure 2. Laser scanner's coordinate system and inertial measurement unit's coordinate system: (a) top view, (b) side view.

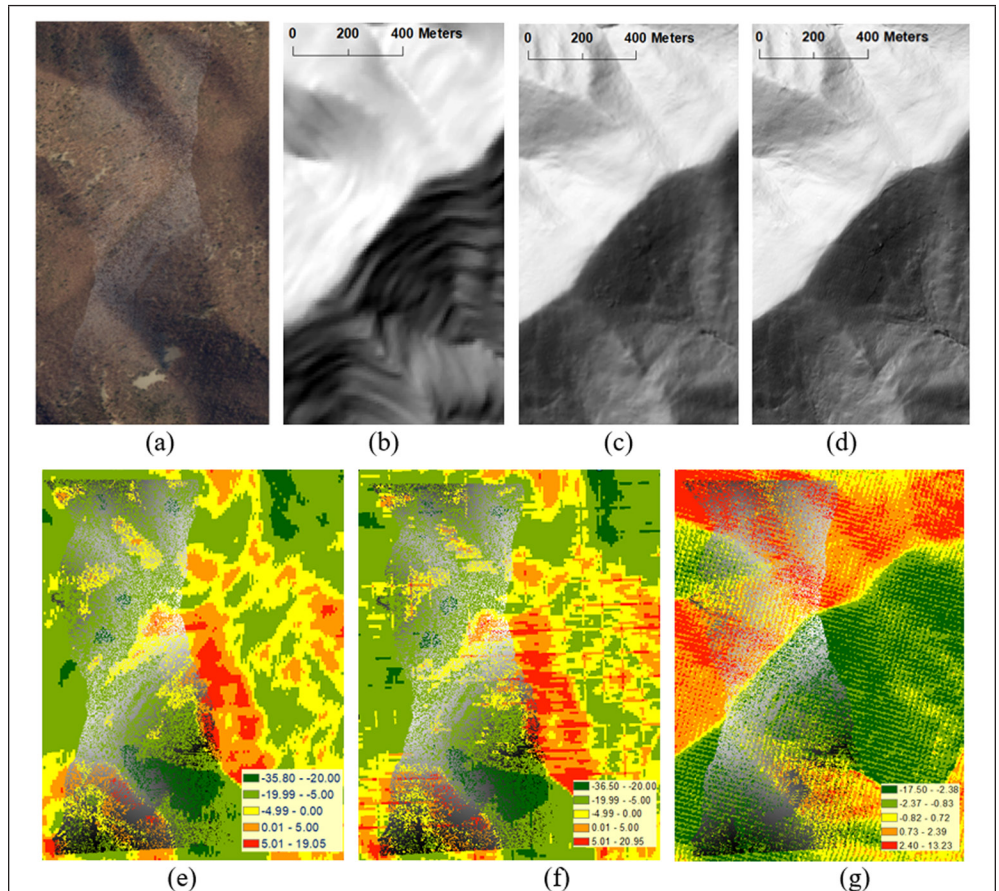


Figure 3. The study area shown in (a) Esri World Imagery, (b-d) the 10-m, 5-m, and 1-m reference digital elevation models (DEMs), respectively; and the difference (in meters) of the pairwise reference DEMs: (e) 10-m DEM - 5-m DEM, (f) 10-m DEM - 1-m DEM, (g) 5-m DEM - 1-m DEM. (a, e-g) The area covered by the waveform lidar points is in gray.

lever arm. In our work, the lever-arm measurement and GPS/INS integration is conducted by the data provider.

The waveform lidar data were collected over a heavy forest area of Shenandoah National Park, VA, USA in June 2011. The study area is about 1430×740 m. Waveform decomposition (Q. Li *et al.* 2016) created a total of 10 580 438 points, with a ground-point density of 1.5 points/m². After initial ground filtering, we were left with 1 285 014 ground points, i.e., a penetration rate of ~12.1%. The density of ground points is about 10 points/m². Figure 3 shows three public DEMs used for our study. The first one is a 10-m DEM obtained from the National Elevation Dataset (U.S. Geological Survey 2013; <http://nationalmap.gov/viewer.html>). The second one is a 5-m DEM obtained from the United States Geological Survey National Geologic Map Database for geological studies in the Paine Run watershed (Chirico 2004). This DEM was derived from airborne lidar data captured using an ALS40 system in 2004. The accuracy of this DEM is ±0.15 m (1 sigma). The third one is a recent 1-m DEM produced through the 3D Elevation Program in 2015–2016 (U.S. Geological Survey 2018; <http://nationalmap.gov/viewer.html>). This hydro-flattened DEM is produced exclusively from high-resolution lidar source data with a nominal pulse spacing of 1 point every 0.7 m. According to Arundel *et al.* (2015), the accuracy of this DEM in vegetated regions is 30 cm (95th percentile).

Ideally, the three reference DEMs should agree with each other where random error/noise is attributed to the resolution. In Figure 3, however, the difference between the 10-m DEM and the other two is obvious. In most of the study area, the 10-m DEM is lower than the 5-m and 1-m DEMs. This may be caused by canopy changes during the two measurements or errors in either of the two data sets. However, this phenomenon reverses in the south-western corner, where the two sides of a ridge have opposite DEM differences. This may be explained by measurement errors, possible canopy changes, or uncalibrated system parameters, such as boresight angles and time synchronization.

Georeferencing Results and Analysis

This section presents and evaluates the results from different stages of the georeferencing computation. Results of direct georeferencing without boresight calibration (Figure 4a), georeferencing with only initial optimization (Figure 4b and c), and final georeferencing with fine optimization (Figure 4d and e) will be discussed.

Direct Georeferencing

In direct georeferencing, the laser scanner and the IMU are assumed to be well aligned so that $[\Delta\omega_0, \Delta\phi_0, \Delta\kappa_0] = [0^\circ, 90^\circ, 90^\circ]$. Also, the system is assumed to be synchronized

such that $\Delta t_0 = 0$ s. Under these assumptions, we have $\theta_0 = [\Delta t_0, \Delta\omega_0, \Delta\phi_0, \Delta\kappa_0] = [0 \text{ s}, 0^\circ, 90^\circ, 90^\circ]$. The generated point cloud (for bare ground) under θ_0 is compared to the 5-m reference DEM, as shown in Figure 4a.

In Figure 4a, repeating linear undulations on the terrain in roughly the east–west direction are observed throughout the study area. It also shows a significant difference between the lidar DEM and the reference DEM. Both the linear undulations and the mean difference of 91.16 m indicate that the boresight calibration and/or the time synchronization was not well performed; some systematic errors exist in the lidar DEM. It is necessary to calibrate both the boresight and the time synchronization based on the objective function described in the previous section. Also, the result in Figure 4a indicates that the start value of θ_0 may be far from its optimal solution, so a global optimization such as particle swarm optimization should be conducted in the initial optimization stage.

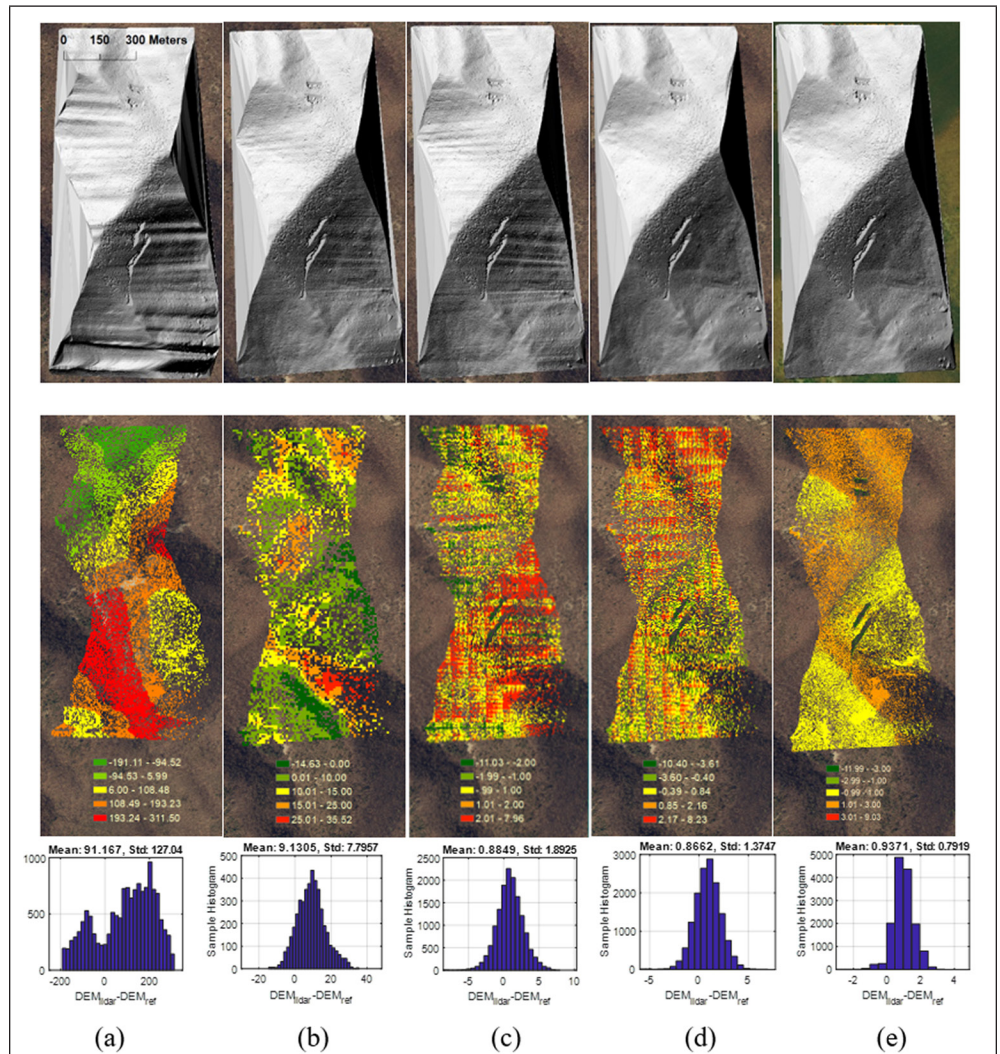


Figure 4. The difference between the resultant lidar digital elevation model (DEM) and a reference DEM from (a) results derived directly from the uncalibrated input (difference is from the 5-m DEM), (b) initial georeferencing with the 10-m DEM as reference, (c) initial georeferencing with the 5-m DEM as reference, (d) final georeferencing with the 5-m DEM as reference, and (e) final georeferencing with the 1-m DEM as reference. The initial georeferencing is from particle swarm optimization, while the final georeferencing is from the subsequent fine optimization. The top row is the hillshaded DEM_{lidar} , the middle row is the DEM difference ($DEM_{lidar} - DEM_{ref}$), and the bottom row is the histogram of the DEM differences.

Initial Georeferencing

During the initial stage, we sampled a total of $N_{\text{init}} = 90\,000$ points in the top, middle, and bottom of the stripe over the study area. The estimation of the parameters $\theta_{\text{init}}^* = [\Delta t_{\text{init}}^*, \Delta \omega_{\text{init}}^*, \Delta \phi_{\text{init}}^*, \Delta \kappa_{\text{init}}^*]$ is obtained by minimizing the objective function $f_{N_{\text{init}}}(\theta_G, \theta_G)$ with particle swarm optimization.

As is shown in Figure 5, we selected three sections of data as the RGC points, distributed across the entire study area, each consisting of 30 000 points. We then conducted two separate experiments by running particle swarm optimization with the 10-m and 5-m reference DEMs separately. We set the number of particles to 40 and the learning factors to 1.5. The computation took about 4 hours on a Dell Precision workstation with eight-core 3.7-GHz CPU and 16-Gb memory. The difference between the lidar DEM and the reference DEMs are calculated. The results are shown in Figure 4b and c.

After particle swarm optimization, the hillshaded DEM is significantly improved, as repeating linear undulations become much less obvious (Figure 4b and c). From the view of DEM differences, the 5-m DEM matches the lidar point clouds better. This is reflected in both the maximum and minimum DEM differences, as shown in the spatial distribution of Figure 4b and c, and the mean difference, as shown in the histogram of Figure 4b and c. In contrast, the difference between the lidar DEM and the 10-m reference DEM has a mean of 9.130 m, which is 10 times higher than the mean difference of 0.885 m between the lidar DEM and the 5-m reference DEM. Since the 10-m DEM reference is significantly different from both our measurement and the other two references, it will be excluded in the next step of optimization.

Comparing Figure 4a and c, we observe that the mean difference between the 5-m reference DEM and the lidar DEM decreases from 91.167 m to 0.885 m. This means that particle swarm optimization has successfully determined the system parameters and reduced most of the deviations between the derived lidar data and the reference DEM. The result shows that the estimated time misalignment is greater than 14.847 s, and the estimated boresight angles deviate by around 1° – 2° from the initial guess. We conclude that the main error before optimization during the direct georeferencing comes from the unaligned time stamps between the laser scanner and POS.

The particle swarm optimization result could be further improved for the following reasons: particle swarm optimization uses a series of random numbers in the search process, which is a good strategy for avoiding the local minimal trap but cannot guarantee that the output result is the global optimal; the performance of the solution is restricted by the number of the RGC points; since the objective function is $f_N(\theta_G, \theta_G)$, the ground filtering process is embedded in each iteration; and in the study area, the forest area has dense leaves so that many lidar signals cannot penetrate the canopy and reach the ground. Since the ground filtering process is embedded in each iteration, errors are inevitable in the filtered ground.

Fine Georeferencing

As the final results, we need to produce the best georeferenced DEMs from the waveform lidar. We use a sampling rate of 1/50 for RGCs and the 1-m reference DEM for calibration. The resultant georeferenced waveform lidar points are used to create a 1-m waveform lidar DEM, which is then compared with the 1-m reference DEM. The results are shown in Figure 4e. Compared to the hillshading in Figure 4a through c, the east-west linear undulations are ultimately removed in Figure 4d and e after the calibration and georeferencing. This demonstrates that our georeferencing framework and solution strategy based on DEM are correct. It also demonstrates that final fine optimization after the initial georeferencing based on selected ground points is necessary. Compared to the resultant DEM of Figure 4d created with reference to the 5-m DEM, the resultant

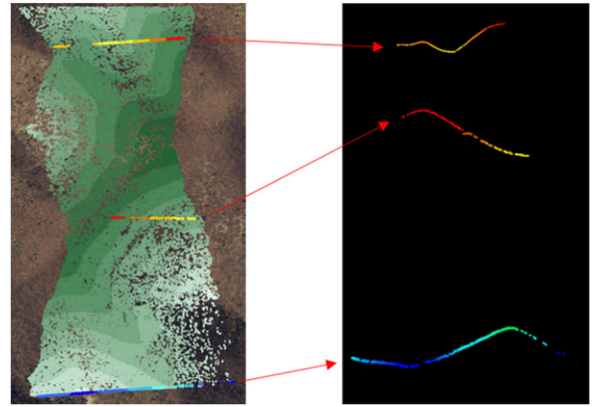


Figure 5. Distribution of the selected $N_{\text{init}} = 3 \times 30\,000$ replacement ground control points used for the initial optimization.

DEM of Figure 4e controlled by the 1-m reference DEM yields a better error distribution, i.e., the percentage of smaller errors is higher than in the 5-m reference DEM. Figure 4e shows that its mean and standard deviation are respectively 0.937 and 0.792 m, which is the best fit among all reference DEMs.

Note that there exists positive bias in our resultant DEMs compared to the reference DEMs, i.e., the waveform lidar-derived DEMs are slightly higher than the reference DEMs. This can be caused by several factors. The reference DEMs are hydrologically corrected such that small undulations and off-ground features are removed. Also, we may not have achieved the best performance of the ground filter (LASTools) when we carried out the ground filtering during the georeferencing process. Furthermore, for heavy canopy areas the waveform lidar may not be powerful enough to penetrate the trees and get returns from the ground. Therefore, some of the ground points we selected through optimization are actually off the ground. All of these factors may yield a DEM that is overall slightly higher than the reference DEM.

Self-Calibration Results and Analysis

This section will discuss the determination of clock offset of the laser scanner with respect to the GPS time and the boresight angles of the laser scanner with respect to the IMU.

Time-Synchronization Offset

In the process of determining synchronization offset, we fix the boresight angles to be $[\Delta \omega_{\text{init}}, \Delta \phi_{\text{init}}, \Delta \kappa_{\text{init}}]$ and carry out the BFGS quasi-Newton algorithm with different initial values of Δt_0 . With the 5-m DEM as the reference, we ran 11 experiments by changing the initial value from 14.50 to 15.50 s with an increment of 0.10 s. Regardless of the initial value, the time misalignment Δt always converges to 15 s. We conclude that $\Delta t_{\text{init}}^* = 15$ s is the stable solution of our synchronization process. On the other hand, the leap seconds of Coordinated Universal Time (UTC) civil time on the day of data collection are 15 s. This means the two instruments use a different system: the GPS/IMU units use GPS time, while the scanner uses UTC time. This has not been considered when deriving the trajectory. We then set $\Delta t = 15.0$ s and conduct the further optimization only for boresight angles.

Boresight Calibration

After the synchronization, the problem of self-calibration is reduced to a problem of boresight optimization on $f_N(\Delta \omega, \Delta \phi, \Delta \kappa)_G; \theta_{\text{init}}^*)$ for a given set of ground points $\{\cdot\}_{N_{\text{gnd}}(\theta_{\text{init}}^*)}$. When

selecting the size of RGC points, we strive for balance between the computational time consumption and the fact that the lidar points should be adequate to reflect the ground shape. In our experiment, we randomly choose an evenly distributed 1/50 of all 1 282 812 ground points in the optimization, so that $N_{\text{grnd}}(\theta_{\text{init}}) = 25\ 637$.

With the starting values $[\Delta\omega_0, \Delta\phi_0, \Delta\kappa_0] = [0^\circ, 90^\circ, 90^\circ]$ and the calibrated time $\Delta t^* = 15$ s, the distribution of RGC points and their distance to the 5-m DEM reference are shown in Figure 6a. In the figure, both the color and the radius of each point are coded by the difference between the lidar-estimated height and the reference height. We can see that the height difference is not evenly distributed: most of the lidar RGC points are lower than the reference DEM in the upper half of the map and higher in the lower half. Figure 6a also shows the histogram of the height differences. It has two peaks, one positive and one negative, which can happen if the system is not well calibrated and the quality of the ground filtering is not perfect.

With the boresight angles obtained from the initial optimization $[\Delta\omega_{\text{init}}^*, \Delta\phi_{\text{init}}^*, \Delta\kappa_{\text{init}}^*] = [-0.8713^\circ, 88.5384^\circ, 91.8591^\circ]$ and the calibrated time $\Delta t^* = 15$ s, the distribution of the RGC points, their height distances to the reference DEM, and the histogram of the height differences are shown in Figure 6b. From both the 2D distribution and the histogram, the height difference is still not evenly distributed. We run the quasi-Newton algorithm to precisely calibrate the boresight angles. The experiments are

repeated 1000 times with random initial values in the range of $\{[\Delta\omega, \Delta\phi, \Delta\kappa]: \Delta\omega \in [-5^\circ, 5^\circ], \Delta\phi \in [-5^\circ, 5^\circ], \Delta\kappa \in [-5^\circ, 5^\circ]\}$. When the initial offset is no greater than 5° from $[0^\circ, 90^\circ, 90^\circ]$, the algorithm converges to $[-0.1561^\circ, 89.0024^\circ, 90.8804^\circ]$, which is the stable solution for our selection of RGC points and is regarded as the final optimal estimation. Figure 6c shows that difference between the lidar RGC points and the reference DEM is overall evenly distributed. The histogram shows that the mean of the height difference is reduced to 0.846 m, with a standard deviation of 0.588 m. To test the stability of the algorithm, we randomly generate another set of RGC points with the same sampling rate of 1/50 and repeat the optimization process from the beginning. The final result shows a similar even spatial distribution and histogram (Figure 6d).

Finally, we further run the algorithm with 5-m and 1-m reference DEMs. For each reference DEM, 30 experiments are conducted with randomly selected RGC points. The initial values for each experiment are set to $[0^\circ, 90^\circ, 90^\circ]$, since this approximation was shown not to affect the convergence of the algorithm. The results are summarized in Table 1.

Table 1 shows that the estimation of the boresight angles is stable with regard to the randomly selected RGC points. For both 5-m and 1-m reference DEMs, the robustness of $\Delta\omega$ and $\Delta\phi$ estimations are stronger, as the standard deviation of both angles is less than 0.003° , while the maximum deviation from the mean value is 0.006° . Being the least sensitive to elevation, the standard deviation of yaw $\Delta\kappa$ is 0.0074° for the 5-m

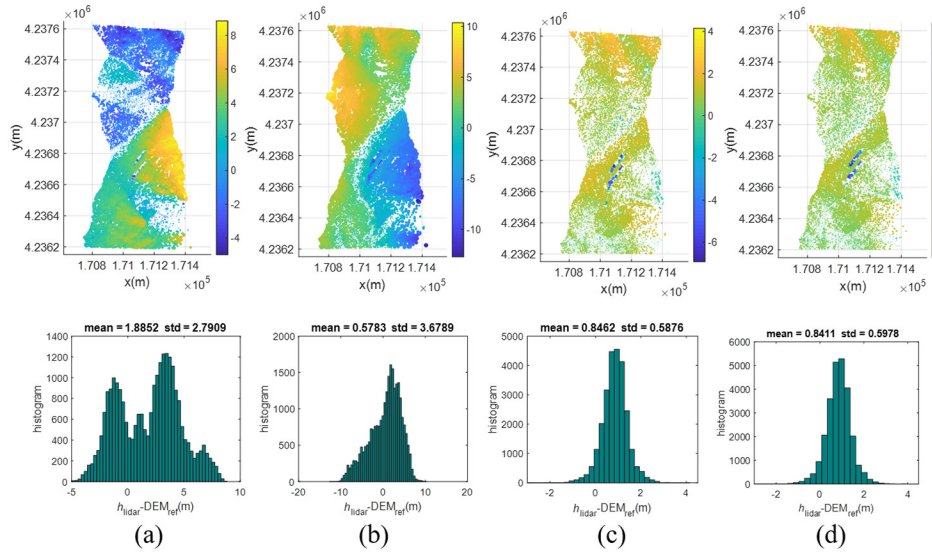


Figure 6. Elevation differences (in m; top) and histogram (bottom) on the replacement ground control points: (a) after the calibration of time synchronization and with the nominal boresight angles of $[0^\circ, 90^\circ, 90^\circ]$; (b) after the calibration of time synchronization and with boresight angles of $[-0.8713^\circ, 88.5384^\circ, 91.8591^\circ]$; (c) the final optimization result; (d) the final result of another set of random replacement ground control points. The reference digital elevation model is the 5-m one.

Table 1. Sensitivity analysis of boresight calibration and georeferencing with different replacement ground control points.

Reference DEM	Statistics	$\Delta\omega(^{\circ})$	$\Delta\phi(^{\circ})$	$\Delta\kappa(^{\circ})$	$\sqrt{\text{MSD}} \text{ (m)}$
5 m	Mean	-0.1564	89.0000	90.8817	1.0240
	SD	0.0015	0.0024	0.0074	0.0035
	Max	-0.1538	89.0059	90.8919	1.0307
	Min	-0.1601	88.9952	90.8643	1.0175
1 m	Mean	-0.1557	89.5522	90.7548	1.1278
	SD	0.0018	0.0024	0.0077	0.0039
	Max	-0.1530	89.5576	90.7673	1.1335
	Min	-0.1604	89.5476	90.7362	1.1176

Total trials = 30; replacement ground control points/total ground points = 1/50.
DEM = digital elevation model.

DEM and 0.0077° for the 1-m DEM, with maximum deviations from the mean value of 0.0186° and 0.0174° , respectively. This result is reasonable, since we virtually only have elevation as control, which is not sensitive to changes in horizontal orientation $\Delta\kappa$.

Another factor that can affect the boresight calibration results is the number of RGC points. We changed the number of randomly selected RGC points to 1/5000, 1/1000, 1/500, 1/100, and 1/50 of the total ground points. In each case, 10 experiments are conducted. The mean values and standard deviations are plotted in Figure 7 and listed in Table 2. The standard deviation of the estimated boresight angles decreases as the number of RGC points increases. When the sampling rate of RGC points reaches 100, or the number of RGC points is greater than 10 000, the mean values of the estimated boresight angles become stable. In practice, the number of RGC points and of tests can be determined according to the specification and requirement of the mission.

Conclusion

This article develops a novel solution for georeferencing airborne full-waveform lidar data and calibrating system parameters by using an existing DEM. The challenge is that no conventional ground control points are available or visible due to canopy coverage. The georeferencing method developed in this article consists of two steps to assure a correct and stable solution. In the first step, we use heuristic optimization

to find a good initial solution to the unknown parameters, including time offset and boresight angles. Particle swarm optimization is tolerant to coarse approximation of the model parameters and can lead to reliable selection of ground points. The second step involves fine optimization (quasi-Newton approach), which is conducted in a small neighborhood of the global optimal solution and is able to achieve refined parameter estimation as the final georeferencing outcome.

Experiments demonstrate that this strategy can resolve both the time synchronization bias and boresight angles with a stable and correct solution under various initial values and selections of ground points for optimization. Compared to the conventional boresight calibration method, which is conducted either by comparing the lidar points with the known ground control points or by co-registering multiple lidar stripes, this approach can significantly reduce the cost of boresight calibration and enable an affordable routine self-calibration simply using existing digital elevation models.

When the model parameters are optimized, the derived georeferenced lidar DEM has an optimal fit to the reference DEM at the selected replacement ground control points under the defined objective function. This optimal fit is rather robust to the selection of RGC points. The variation of the objective function is only a couple of centimeters when the number of RGC points varies from several hundreds to tens of thousands. Correspondingly, the differences between the lidar-derived DEM and the reference DEM are stable, with a mean of 0.937 m and a standard deviation of 0.792 m. The quality of the

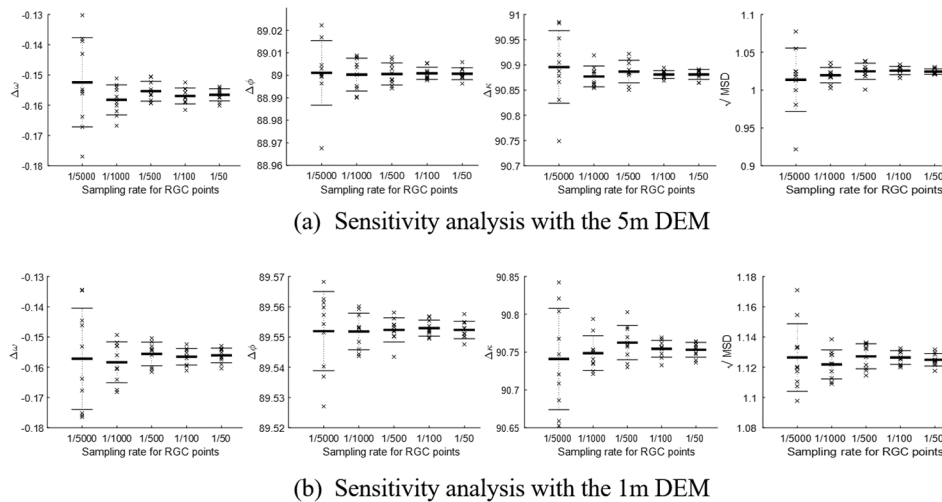


Figure 7. Sensitivity analysis of the estimated boresight angles ($^\circ$) and the objective function values (m). In each plot, the mean value is plotted as a heavy bar, the standard deviation as light bar, and the estimated values of each individual experiment as crosses.

Table 2. Results of boresight calibration with different numbers of replacement ground points (RGCs).

Reference DEM	RGC Sampling Rate	Number of RGC Points	Estimation Results: Mean (SD)			
			$\Delta\omega(^{\circ})$	$\Delta\phi(^{\circ})$	$\Delta\kappa(^{\circ})$	$\sqrt{\text{MSD}} \text{ (m)}$
5 m	1/5000	256	-0.1524 (0.0147)	89.0011 (0.0144)	90.8957 (0.0718)	1.0136 (0.0419)
	1/1000	1,282	-0.1582 (0.0050)	89.0003 (0.0073)	90.8770 (0.0209)	1.0197 (0.0102)
	1/500	2,565	-0.1554 (0.0033)	89.0006 (0.0049)	90.8867 (0.0223)	1.0248 (0.0108)
	1/100	12,828	-0.1569 (0.0026)	89.0009 (0.0027)	90.8809 (0.0081)	1.0258 (0.0052)
	1/50	25,637	-0.1566 (0.0020)	89.0007 (0.0026)	90.8811 (0.0099)	1.0245 (0.0036)
1 m	1/5000	256	-0.1572 (0.0167)	89.5519 (0.0131)	90.7409 (0.0669)	1.1265 (0.0223)
	1/1000	1,282	-0.1584 (0.0067)	89.5518 (0.0060)	90.7486 (0.0230)	1.1219 (0.0096)
	1/500	2,565	-0.1556 (0.0039)	89.5523 (0.0040)	90.7626 (0.0225)	1.1272 (0.0083)
	1/100	12,828	-0.1565 (0.0028)	89.5529 (0.0026)	90.7544 (0.0111)	1.1264 (0.0045)
	1/50	25,656	-0.1561 (0.0024)	89.5523 (0.0029)	90.7531 (0.0098)	1.1250 (0.0042)

DEM = digital elevation model.

resultant DEM depends on the quality of the reference DEM and the ability to reveal the ground from the waveform lidar data. Under heavy canopy, waveform lidar may not have full penetration to the ground in all places. Similarly, the ground filtering may not perform perfectly. The resultant DEM may therefore be slightly biased from the reference DEM.

There are limitations for this method. Since the reference DEM is utilized as ground control, no significant terrain change should happen after its collection and before the lidar measurement. This assumption may not hold if such terrain changes as erosion or landslide occur in the study area. Moreover, as we are essentially minimizing the fitting errors between two bare-ground terrain models, the definition of the terrain has to be consistent, which sometimes can be ambiguous for different landscapes and when different ground filters are used. Blunder detection might be incorporated as part of the georeferencing process if the reference DEM is over complex terrain or has undergone certain complicated processing, such as hydrological correction. Furthermore, the performance of this approach may be further investigated for different types of terrain, especially when it is relatively flat, since that may cause large georeferencing uncertainty.

Finally, it should be noted that this approach is also applicable with little adaption to the calibration and georeferencing of conventional discrete lidar for urban or suburban areas. Under such scenarios, one may not need to carry out ground filtering to get the bare ground. Instead, an existing digital surface model can be used as the reference to which the lidar points are georeferenced. It is a simplified version of the presented approach; however, extension is necessary when typical urban features are added into this optimization process, to possibly improve its performance.

Acknowledgments

The work was in part sponsored by the Army Research Office. Peter G. Chirico at the United States Geological Survey provided information about the 5-m reference DEM. Ruya Xu contributed to the revision of the manuscript.

References

- Arundel, S. T., C.-A. M. Archuleta, L. A. Phillips, B. L. Roche and E. W. Constance. 2015. 1-meter digital elevation model specification. In : *U.S. Geological Survey Techniques and Methods*, book 11, chapter B7. Reston, Va.: U.S. Geological Survey.
- Axelsson, P. 2000. DEM generation from laser scanner data using adaptive TIN models. *The International Archives of the Photogrammetry, Remote Sensing and Spatial Information Sciences*, XXXIII (B4):110–117.
- Broyden, C. G. 1970. The convergence of a class of double-rank minimization algorithms: 1. General considerations. *IMA Journal of Applied Mathematics* 6 (1):76–90.
- Cao, H., P. Tao, H. Li and J. Shi. 2019. Bundle adjustment of satellite images based on an equivalent geometric sensor model with digital elevation model. *ISPRS Journal of Photogrammetry and Remote Sensing* 156:169–183.
- Chen, S., H. Ma, Y. Zhang, L. Zhong, J. Xu and H. Chen. 2012. Bore-sight calibration of airborne LiDAR system without ground control points. *IEEE Geoscience and Remote Sensing Letters* 9 (1):85–89.
- Chirico, P. G. 2004. *LIDAR derived 5m resolution bare earth and first return digital elevation model of the Paine Run Watershed, Augusta County, Virginia*. Open-File Report 2004-1320.
- Cortes, C., M. Shahbazi and P. Ménard. 2018. UAV-LiCAM system development: Calibration and geo-referencing. *The International Archives of the Photogrammetry, Remote Sensing and Spatial Information Sciences* XLII (1):107–114.
- Csanyi, N. and C. K. Toth. 2007. Improvement of lidar data accuracy using lidar-specific ground targets. *Photogrammetric Engineering and Remote Sensing* 73 (4):385–396.
- Fletcher, R. 1970. A new approach to variable metric algorithms. *The Computer Journal* 13 (3):317–322.
- Golbon-Haghighi, M. H., H. Saeidi-Manesh, G. Zhang and Y. Zhang. 2018. Pattern synthesis for the Cylindrical Polarimetric Phased Array Radar (CPPAR). *Progress in Electromagnetics Research* 66:87–98.
- Goldfarb, D. 1970. A family of variable-metric methods derived by variational means. *Mathematics of Computation* 24 (109):23–26.
- Guo, Q., Y. Su, T. Hu, X. Zhao, F. Wu, Y. Li, J. Liu, L. Chen, G. Xu, G. Lin, Y. Zheng, Y. Lin, X. Mi, L. Fei and X. Wang. 2017. An integrated UAV-borne lidar system for 3D habitat mapping in three forest ecosystems across China. *International Journal of Remote Sensing* 38 (8–10):2954–2972.
- Hancock, S., J. Armston, Z. Li, R. Gaulton, P. Lewis, M. Disney, F. M. Danson, A. Strahler, C. Schaaf, K. Anderson and K. J. Gaston. 2015. Waveform lidar over vegetation: An evaluation of inversion methods for estimating return energy. *Remote Sensing of Environment* 164:208–224.
- Hebel, M. and U. Stilla. 2012. Simultaneous calibration of ALS systems and alignment of multiview LiDAR scans of urban areas. *IEEE Transactions on Geoscience and Remote Sensing* 50 (6):2364–2379.
- Jung, J., J. Kim, S. Yoon, S. Kim, H. Cho, C. Kim and J. Heo. 2015. Bore-sight calibration of multiple laser range finders for kinematic 3D laser scanning systems. *Sensors* 15 (5):10292–10314.
- Kenney, J., 1995. Particle swarm optimization. In *Proc. IEEE International Conference on Neural Networks*, pp. 1942–1948.
- Le Gentil, C., T. Vidal-Calleja and S. Huang. 2018. 3D LiDAR-IMU calibration based on upsampled preintegrated measurements for motion distortion correction. Pages 2149–2155 in *2018 IEEE International Conference on Robotics and Automation (ICRA)*, held in Brisbane, Australia, 21–25 May 2018. Edited by J. Editor. City, St.: IEEE.
- Li, C., J. Liu, X. Wang, X. Liu and Y. Wu. 2018. Stepwise-then-intelligent algorithm (STIA) for optimizing remotely sensed image rectification. *International Journal of Remote Sensing* 39 (21):7350–7369.
- Li, Q., J. Degnan, T. Barrett and J. Shan. 2016. First evaluation on single photon-sensitive lidar data. *Photogrammetric Engineering and Remote Sensing* 82 (7):455–463.
- Li, Q., S. Ural, J. Anderson and J. Shan. 2016. A fuzzy mean-shift approach to lidar waveform decomposition. *IEEE Transactions on Geoscience and Remote Sensing* 54 (12):7112–7121.
- Li, Q., S. Ural and J. Shan. 2016. Decomposing LiDAR waveforms with nonparametric classification methods. Pages 5573–576 in *2016 IEEE International Geoscience and Remote Sensing Symposium (IGARSS)*, held in Beijing, China, 10–15 July 2016. Edited by J. Editor. City, St.: IEEE.
- Li, Q., S. Ural and J. Shan. 2018. A comparative study on airborne lidar waveform decomposition methods. Pages 1–6 in *2018 10th IAPR Workshop on Pattern Recognition in Remote Sensing (PRRS)*, held in Beijing, China, 19–20 August 2018. Edited by J. Editor. City, St.: IEEE.
- Liu, W. 2017. LiDAR-IMU time delay calibration based on iterative closest point and iterated sigma point Kalman filter. *Sensors* 17 (3):539.
- Liu, W. I. and Y. Li. 2019. Error modeling and extrinsic-intrinsic calibration for LiDAR-IMU system based on cone-cylinder features. *Robotics and Autonomous Systems* 114:124–133.
- Luo, X., Q. Liu and Q. Liu. 2010. Exterior orientation elements' Bayesian estimation model under insufficient ground control points. Pages 1–5 in *2010 18th International Conference on Geoinformatics*, held in Beijing, China, 18–20 June 2010. Edited by J. Editor. City, St.: IEEE.
- Morales, J., J. L. Martínez, A. Mandow, A. J. Reina, A. Pequeño-Boer and A. García-Cerezo. 2014. Bore-sight calibration of construction misalignments for 3D scanners built with a 2D laser rangefinder rotating on its optical center. *Sensors* 14 (11):20025–20040.

- Nagarajan, S. and S. Moafipoor. 2018. Boresight calibration of low point density lidar sensors. *Photogrammetric Engineering and Remote Sensing* 84 (10):619–627.
- Pan, Z., P. Hartzell and C. Glennie. 2017. Calibration of an airborne single-photon lidar system with a wedge scanner. *IEEE Geoscience and Remote Sensing Letters* 14 (8):1418–1422.
- Pirotti, F. 2011. Analysis of full-waveform LiDAR data for forestry applications: A review of investigations and methods. *iForest-Biogeosciences and Forestry* 4 (3):100–106.
- Poli, R. 2008. Analysis of the publications on the applications of particle swarm optimisation. *Journal of Artificial Evolution and Applications* 2008:685175.
- Pothou, A., C. Toth, S. Karamitsos and A. Georgopoulos. 2008. An approach to optimize reference ground control requirements for estimating LiDAR/IMU boresight misalignment. *The International Archives of the Photogrammetry, Remote Sensing and Spatial Information Sciences XXXVII (B1)*:301–307.
- Shan, J. 2001. An approach to single image automatic orientation and point determination by using orthoimages and a DTM. *The Photogrammetric Record* 17 (98):343–353.
- Shan, J. and C. Toth. 2018. *Topographic Laser Ranging and Scanning: Principles and Processing*, 2nd ed. Boca Raton, Fla.: CRC Press.
- Shanno, D. F. 1970. Conditioning of quasi-Newton methods for function minimization. *Mathematics of Computation* 24 (111):647–656.
- Skaloud, J. and D. Lichti. 2006. Rigorous approach to bore-sight self-calibration in airborne laser scanning. *ISPRS Journal of Photogrammetry and Remote Sensing* 61 (1):47–59.
- Skaloud, J. and P. Schaer. 2007. Towards automated LiDAR boresight self-calibration. Pages PP–PP in *Proceedings of 5th International Symposium on Mobile Mapping Technology*, held in Padova, Italy, 29–31 May 2007. Edited by J. Editor. City, St.: Publisher.
- Sun, X. and G. A. Neumann. 2015. Calibration of the Mercury Laser Altimeter on the MESSENGER spacecraft. *IEEE Transactions on Geoscience and Remote Sensing* 53 (5):2860–2874.
- Toth, C. K., N. Csanyi and D. A. Grejner-Brzezinska. 2002. Automating the calibration of airborne multisensor imaging systems. Pages PP–PP in *Proceedings ACSM-ASPRS Annual Conference*, held in Washington, D.C., 19–26 April 2002. Edited by J. Editor. City, St.: Publisher.
- U.S. Geological Survey. 2013. *USGS NED n39079 1/3 arc-second 2013 1x1 degree IMG*. Reston, Va.: U.S. Geological Survey.
- U.S. Geological Survey. 2018. *USGS NED one meter x69y424 VA ChesapeakeBayNorth 2015 IMG 2018*. Reston, Va.: U.S. Geological Survey.
- White, J. C., N. C. Coops, M. A. Wulder, M. Vastaranta, T. Hilker and P. Tompalski. 2016. Remote sensing technologies for enhancing forest inventories: A review. *Canadian Journal of Remote Sensing* 42 (5):619–641.
- Wu, B. and W. C. Liu. 2017. Calibration of boresight offset of LROC NAC imagery for precision lunar topographic mapping. *ISPRS Journal of Photogrammetry and Remote Sensing* 128:372–387.
- Zhang, Y., X. Xiong, M. Zheng and X. Huang. 2015. LiDAR strip adjustment using multifeatures matched with aerial images. *IEEE Transactions on Geoscience and Remote Sensing* 53 (2):976–987.
- Zhu, Q., J. Wu, H. Hu, C. Xiao and W. Chen. 2018. LIDAR point cloud registration for sensing and reconstruction of unstructured terrain. *Applied Sciences* 8 (11):2318.